



**HAL**  
open science

## Modeling Soft X-Ray Emissions at the Dayside Magnetopause

Qiuyu Xu, Dimitra Koutroumpa, Ronan Modolo, Tianran Sun, Hyunju  
Connor, Steve Sembay, Yevhen Tkachenko

► **To cite this version:**

Qiuyu Xu, Dimitra Koutroumpa, Ronan Modolo, Tianran Sun, Hyunju Connor, et al.. Modeling Soft X-Ray Emissions at the Dayside Magnetopause. *Journal of Geophysical Research Space Physics*, 2024, 129 (8), pp.e2024JA032687. 10.1029/2024ja032687 . insu-04678681

**HAL Id: insu-04678681**

**<https://insu.hal.science/insu-04678681v1>**

Submitted on 27 Aug 2024

**HAL** is a multi-disciplinary open access archive for the deposit and dissemination of scientific research documents, whether they are published or not. The documents may come from teaching and research institutions in France or abroad, or from public or private research centers.

L'archive ouverte pluridisciplinaire **HAL**, est destinée au dépôt et à la diffusion de documents scientifiques de niveau recherche, publiés ou non, émanant des établissements d'enseignement et de recherche français ou étrangers, des laboratoires publics ou privés.



Distributed under a Creative Commons Attribution 4.0 International License

# JGR Space Physics

## RESEARCH ARTICLE

10.1029/2024JA032687

## Modeling Soft X-Ray Emissions at the Dayside Magnetopause



### Key Points:

- 3D global LATmos TEst Particle (LaTeP) model is applied to simulate the soft X-ray emissions at dayside magnetosheath and the cusps
- The kinetic effects and the individual spectral characteristics that LaTeP model introduces are investigated
- The map of OVII over OVIII line ratios reveals a distinguished boundary at the bow shock

### Supporting Information:

Supporting Information may be found in the online version of this article.

### Correspondence to:


Q. Xu,  
[qiuyu.xu@latmos.ipsl.fr](mailto:qiuyu.xu@latmos.ipsl.fr)

### Citation:

Xu, Q., Koutroumpa, D., Modolo, R., Sun, T., Connor, H., Sembay, S., & Tkachenko, Y. (2024). Modeling soft X-ray emissions at the dayside magnetopause. *Journal of Geophysical Research: Space Physics*, 129, e2024JA032687. <https://doi.org/10.1029/2024JA032687>

Received 27 MAR 2024

Accepted 8 AUG 2024

Qiuyu Xu<sup>1</sup> , Dimitra Koutroumpa<sup>1</sup> , Ronan Modolo<sup>1</sup> , Tianran Sun<sup>2</sup> , Hyunju Connor<sup>3</sup> , Steve Sembay<sup>4</sup> , and Yevhen Tkachenko<sup>5</sup> 

<sup>1</sup>LATMOS/IPSL, CNRS, UVSQ Université Paris-Saclay, Sorbonne Université, Guynacourt, France, <sup>2</sup>National Space Science Center, Chinese Academy of Sciences, Beijing, China, <sup>3</sup>NASA Goddard Space Flight Center, Greenbelt, MD, USA, <sup>4</sup>Leicester University, Leicester, UK, <sup>5</sup>Sorbonne Université, Observatoire de Paris, PSL Research University, LERMA, CNRS UMR, Paris, France

**Abstract** In this study, we simulate the Solar Wind Charge Exchange (SWCX) soft X-ray emissions at dayside magnetosheath and cusps by using magnetohydrodynamic (MHD) and LATmos TEst Particle (LaTeP) models. MHD models are unable to resolve the particle kinetic effects, such as the different behaviors of ions with different  $q/m$ , or distinguish the magnetospheric plasma from the solar wind plasma. We investigate these effects with the LaTeP model. As the LaTeP model does not self-compute magnetic and electric field, the magnetic and electric field data obtained from Open Geospace General Circulation Model (OpenGGCM) and Lagrangian version of the piecewise parabolic method (PPMLR) MHD model are used as the input to LaTeP model. The soft X-ray emissivity maps simulated from pure OpenGGCM and PPMLR MHD approaches and from LaTeP-OpenGGCM and LaTeP-PPMLR approaches are presented and compared. The results indicate that the LaTeP model can well resolve the kinetic effects and can be used to investigate the individual spectral characteristics. Therefore, the LaTeP model is a complementary approach for simulating the X-ray emissions near the dayside magnetopause. We also calculate the ratio of integrated OVII/OVIII line intensities, produced by charge exchange of  $O^{7+}$  ions and  $O^{8+}$  ions, respectively. We find a relatively higher ratio at the bow shock compared to the surrounding areas, suggesting that this ratio can be an effective parameter to identify the bow shock location.

**Plain Language Summary** At the magnetopause, X-ray emissions are generated by charge exchange reactions between multiply charged heavy solar wind ions and the neutral hydrogen atoms in the geocorona. In this study, we simulate the soft X-ray emissions around the Earth by using magnetohydrodynamic (MHD) and LATmos TEst Particle (LaTeP) model. As the LaTeP model requires external magnetic and electric field input, we use the magnetic and electric field data obtained from OpenGGCM and PPMLR MHD model as its input. Then the simulation results from pure OpenGGCM and PPMLR MHD approaches and from LaTeP-OpenGGCM and LaTeP-PPMLR approaches are presented and compared. The comparison indicates that the LaTeP model can well resolve particle kinetic effects and individual spectral features. Therefore, the LaTeP model is a complementary approach for simulating the X-ray emissions in Earth's magnetopause. The maps of the ratio of spectral lines produced by  $O^{7+}$  ions and  $O^{8+}$  ions are also calculated. At the bow shock, this ratio is higher than that of the surrounding areas, indicating it is an effective parameter to identify the bow shock.

## 1. Introduction

The Earth's magnetopause is a boundary separating the magnetosphere and the magnetosheath, which is formed through the interaction of the solar wind with the terrestrial magnetic field. Since the first observations of the magnetopause in 1960s (Cahill & Amazeen, 1963), various magnetopause crossing events of spacecrafts are widely reported and studied (e.g., Haaland et al., 2019; Samsonov et al., 2021; Trattner et al., 2020). However, a comprehensive understanding of the global responses and evolution of the magnetopause remains challenging due to data limitations from in situ spacecraft observations. Measuring soft X-ray emissions from solar wind charge exchange (SWCX) is a good approach to remotely detect the interactions between solar wind and magnetosphere, as well as the corresponding response of the magnetopause (Connor et al., 2021; J. Guo et al., 2023; Walsh et al., 2016; Zhang et al., 2022).

© 2024 The Author(s).

This is an open access article under the terms of the [Creative Commons Attribution-NonCommercial License](https://creativecommons.org/licenses/by-nc/4.0/), which permits use, distribution and reproduction in any medium, provided the original work is properly cited and is not used for commercial purposes.

At the magnetopause, X-ray emissions are generated by charge exchange reactions between multiply charged heavy solar wind ions ( $O^{7+}$ ,  $C^{5+}$ , ...) and the neutral particles (mostly hydrogen atoms) in the geocorona. This interaction can be given in Equation 1,



where the heavy and multiply charged ( $q+$ ) solar wind ion is noted as  $X^{q+}$  and the neutral particle is noted as  $M$ . Electrons are transferred from neutral particles to ions and causes these ions into an excited state. When the excited ions return to the lower-energy state, they will shortly emit photons in the soft X-ray band ( $E \leq 2$  keV):



Equations 1 and 2 can be considered as the basic process of SWCX X-ray emissions observed at various objects in the Solar System. SWCX emissions have now been observed around comets (Lisse et al., 1996; Mullen et al., 2017; Wedlund et al., 2020) and planetary bodies such as Mars, Venus, Moon, Jupiter (Collier et al., 2014; Dennerl, 2008; Dunn et al., 2022), and Earth (Carter et al., 2010; Cravens et al., 2001; Fujimoto et al., 2007; Ishikawa et al., 2013; Liang et al., 2023; Zhang et al., 2023).

The soft X-ray emissions observed in the dayside magnetosheath and cusps are typically strong, due to the high density of solar wind ions and neutral particles in these regions. On the contrary, a very low density of solar wind ions in the magnetosphere and a very low density of neutral hydrogen atoms in the solar wind lead to weak soft x-ray emissions in these two regions. Therefore, there is expected to be a distinguished boundary at the magnetopause in terms of soft X-ray emissivity. This increase of soft X-ray emission at the boundary should allow us to derive the location of the magnetopause through global soft X-ray imaging with space-born instruments. Such imaging will be possible with the forthcoming Solar wind Magnetosphere Ionosphere Link Explorer (SMILE) mission, which is a joint European Space Agency (ESA) and Chinese Academy of Sciences (CAS) mission and scheduled for launch in 2025 (Branduardi-Raymont et al., 2018; Wang & Branduardi-Raymont, 2018). The Soft X-ray Imager (SXI) onboard SMILE has a wide field of view ( $15.5^\circ \times 26.5^\circ$ ), thus can remotely obtain the global soft X-ray images of the magnetosheath and cusps, which will allow us to investigate the interaction between the solar wind and the magnetosphere (Sembay et al., 2023).

Given the current absence of the large-scale X-ray images near the magnetopause, it is important to conduct simulations of soft X-ray emissions in the magnetosheath and cusps. This preparatory step will help to effectively analyze the expected images from the forthcoming SMILE mission. Robertson and Cravens (2003) first simulated X-ray images of the magnetosheath based on the model of SWCX X-ray emissions developed by Cravens et al. (2001). Robertson et al. (2006) simulated X-ray emissions for a geomagnetic storm event by using solar wind parameters taken from magnetohydrodynamic (MHD) simulations. Whittaker et al. (2016) used MHD model to simulate the SWCX X-ray emissions and compare with XMM-Newton observations. The MHD model was also used to simulate the response of X-ray images to various solar wind conditions (Connor et al., 2021; Sun et al., 2019). Then methods for analyzing X-ray images to derive the magnetopause position were developed based on MHD simulation results (Collier & Connor, 2018; Cucho-Padin et al., 2023; Y. Guo et al., 2022; Kim et al., 2023; Samsonov, Sembay, et al., 2022; Sun et al., 2020). Sibeck et al. (2018) reviewed efforts to image the diagnostic plasma density structures in the SWCX soft X-ray emissions.

However, one of the fundamental problems is that the MHD model describes the plasma as a single fluid, which results in certain limitations. Firstly, the MHD models are unable to resolve the inhomogeneities caused by particle kinetic effects in the magnetosheath. Secondly, the MHD models cannot distinguish the magnetospheric plasma and the solar wind plasma, and the density in the magnetosphere predicted by MHD models is artificially higher than the observation. This means a masking method is needed to separate the magnetosphere from the magnetosheath and cusps (Kuntz et al., 2015; Samsonov, Carter, et al., 2022). To address these limitations, other models such as the hybrid-PIC simulation model (Grandin et al., 2023; J. Guo et al., 2023; Ng et al., 2023) or the test particle model (Koutroumpa et al., 2012) (an early version of the LATmos TESt Particle (LaTeP) model in this paper) should be considered. The LaTeP model is based on a test particle Monte Carlo approach under given magnetic and electric field, allowing the LaTeP model to study the kinetic effects and distinguish the magnetospheric plasma originated from the solar wind. Since the heavy and multiply charged solar wind ions represent a

minor contribution to the SW composition, their impact on the current system is negligible and we can assume that the electric and magnetic field will not be affected by these ion species. The consistency of LaTeP simulations has already been shown in works on Mars (Koutroumpa et al., 2012) and Earth (Tkachenko et al., 2021). Therefore, it is necessary to simulate SWCX X-ray emission of the turbulent environment and investigate particle kinetic effects on the X-ray images by using the LaTeP model.

In this study, we perform 3D global LaTeP simulations under southward Interplanetary Magnetic Field (IMF) to estimate the soft X-ray emissions of the Earth's magnetosheath and cusps. As the LaTeP model requires external magnetic and electric field input, we use the magnetic and electric field data obtained from OpenGGCM and PPMLR MHD models as the input of LaTeP model. Then the soft X-ray emissions from pure OpenGGCM and PPMLR MHD approaches and from LaTeP-OpenGGCM and LaTeP-PPMLR MHD approaches are presented and compared. Our goal is not to compare in detail the two MHD inputs but rather validate the results of the LaTeP approach under various inputs. The methods and simulation models used in this paper are described in Section 2. In Section 3, we present the LaTeP simulation results and pure MHD simulation results. The discussion and conclusion are presented in Section 4 and Section 5, respectively.

## 2. Methods

The SWCX emission consists of distinct spectral lines characteristic of the generated ions  $X^{(q-1)+}$ . The volume emissivity of X-ray Q is in the unit of  $\text{eV cm}^{-3} \text{s}^{-1}$  and can be calculated as:

$$Q = n_M \cdot n_{X^{q+}} \cdot v_{X^{q+}} \cdot \sigma_{X^{q+},M} \cdot Y_{X^{(q-1)+}}, \quad (3)$$

where  $n_M$  indicates the neutral density,  $n_{X^{q+}}$  indicates the source ion density,  $v_{X^{q+}}$  indicates the plasma velocity,  $\sigma_{X^{q+},M}$  indicates the cross-section of the collision, and  $Y_{X^{(q-1)+}}$  indicates the emission line energy weighted by the emission probability of each transition. In the simulation,  $n_M$ ,  $n_{X^{q+}}$ ,  $v_{X^{q+}}$ ,  $\sigma_{X^{q+},M}$ , and  $Y_{X^{(q-1)+}}$  are calculated in the unit of  $\text{cm}^{-3}$ ,  $\text{cm}^{-3}$ ,  $\text{cm s}^{-1}$ ,  $\text{cm}^2$  and eV, respectively. The  $\sigma_{X^{q+},M}$  are calculated from the KRONOS (<https://sites.physast.uga.edu/ugacxdb/>) database (Cumbee et al., 2021) and emission probabilities are based on studies of Kharchenko and Dalgarno (2000), Kharchenko (2005), Koutroumpa et al. (2006). Note that  $\sigma_{X^{q+},M}$  and  $Y_{X^{(q-1)+}}$  is velocity- and species-dependent. However, in the velocity range in the simulations investigated in this paper, the impact of the velocity-dependence is not deemed significant. We use MHD and LaTeP model to simulate the SWCX soft X-ray emissions and derive the corresponding volume emissivity  $Q_{\text{MHD}}$  and  $Q_{\text{LaTeP}}$ .

### 2.1. MHD Model

OpenGGCM is a global magnetosphere–ionosphere (MI) MHD model. It divides the Earth's geospace system into two regions—the magnetosphere and the MI coupling zone. For the outer magnetosphere, OpenGGCM solves resistive MHD equations in the non-uniform Cartesian grids with current-driven resistivities in addition to numerical resistivities. The simulation domain used in this study is  $-100 R_E < X < 20 R_E$ ,  $-45 R_E < Y < 45 R_E$  and  $-45 R_E < Z < 45 R_E$ . The inner boundary of OpenGGCM is set at a geocentric distance of  $3.5 R_E$  because the MHD physics are no longer applicable in this region. For the MI coupling zone, OpenGGCM couples a 3D magnetosphere with a 2D high-latitude ionosphere, assuming that the field-aligned currents created by the solar wind–magnetosphere interaction are closed in the ionosphere (Raeder et al., 2008).

The PPMLR model simulates the MI system using the Piecewise Parabolic Method with a Lagrangian remap algorithm (Hu et al., 2007). The simulation domain also has two regions. For the magnetosphere region, MHD equations are calculated by using an extension of the PPMLR algorithm to MHD developed by Colella and Woodward (1984). The simulation domain is  $-100 R_E < X < 30 R_E$ ,  $-100 R_E < Y < 100 R_E$  and  $-100 R_E < Z < 100 R_E$ , with an inner boundary at a spherical shell with  $r = 3 R_E$ . For the MI coupling region, the coupling in the PPMLR model consists of a mapping of field-aligned currents from the inner magnetosphere to the ionosphere as well as the electric potential in the opposite direction, both along the Earth's dipole field lines. The ionospheric electric potential equation is calculated on a spherical shell with  $r = 1.017 R_E$ , which is the typical geocentric distance for the ionosphere.

As the LaTeP model needs external magnetic and electric field input, we use the magnetic and electric field data obtained from OpenGGCM and PPMLR MHD models as the input to LaTeP model. The OpenGGCM and

**Table 1**  
The Solar Wind Parameters Used in OpenGGCM and PPMLR MHD Model

MHD model	$V_x$ (km s <sup>-1</sup> )	$B_z$ (nT)	$n$ (cm <sup>-3</sup> )
OpenGGCM PPMLR	-400	-5	12.5

PPMLR models have been used to estimate the SWCX X-ray emissions from the magnetosheath in Connor et al. (2021) and Sun et al. (2019), respectively, under various solar wind conditions. In this paper we assume the same southern IMF solar wind conditions for both MHD models. The main solar wind parameters used in the OpenGGCM and PPMLR models in geocentric solar magnetospheric (GSM) coordinate system are listed in Table 1. Other solar wind parameters are all zero:  $V_y = V_z = 0$  km s<sup>-1</sup>,  $B_x = B_y = 0$  nT. And the dipole tilt angle of the Earth's magnetic field is set to be zero in both MHD models. The magnetic field  $B_z$ , electric field  $E_y$ , density, velocity  $V_x$  and pressure results obtained from OpenGGCM and PPMLR models are presented in Figures S1–S5 of Supporting Information S1. Although the overall behaviors of the two MHD models are similar under the same upstream conditions, the discrepancy between the two MHD models' outputs can occur due to the difference in simulation grids, resistivities used in the MHD equations, initial settings of geospace systems before the simulation run (e.g., plasmasphere and ionosphere) and MI coupling techniques, etc. The differences between the OpenGGCM and PPMLR models indicate the uncertainty of MHD results. In particular, note that the two models produce magnetopause stand-off distances that are different by over 1  $R_E$ . The electro-magnetic field data obtained from OpenGGCM and PPMLR models are interpolated to the near-Earth region of  $0 R_E < X < 20 R_E$ ,  $-10 R_E < Y < 10 R_E$ ,  $-10 R_E < Z < 10 R_E$ , with the grid spacing of  $0.05 R_E$ . These interpolated electro-magnetic field data are then used as the input to LaTeP model.

The X-ray volume emissivity can be calculated from pure MHD approach based on Equation 3:

$$Q_{\text{MHD}} = n_{\text{H}} \cdot n_{\text{X}^{q+}} \cdot v_{\text{X}^{q+}} \cdot \sigma_{\text{X}^{q+},\text{H}} \cdot Y_{\text{X}^{(q-1)+}}, \quad (4)$$

where  $n_{\text{X}^{q+}}$  can be calculated from  $n_{\text{H}^+} \cdot \left[ \frac{\text{X}^{q+}}{\text{O}} \right] \cdot \left[ \frac{\text{O}}{\text{H}^+} \right]$ , and  $v_{\text{X}^{q+}}$  can be considered the same as  $v_{\text{H}^+}$ . Here  $\left[ \frac{\text{X}^{q+}}{\text{O}} \right]$  indicates the relative abundance of the species  $\text{X}^{q+}$  with respect to oxygen O, and  $\left[ \frac{\text{O}}{\text{H}^+} \right]$  indicates the abundance of oxygen with respect to solar wind protons. Hence, the equation can be simplified as:

$$Q_{\text{MHD}} = \alpha_{\text{H}} \cdot n_{\text{H}} \cdot n_{\text{H}^+} \cdot v_{\text{H}^+}, \quad (5)$$

where  $\alpha_{\text{H}}$  is a combined coefficient that contains the atomic physics parameters (cross sections and emission probabilities) relative to each ion in the solar wind, as well as the composition properties of the solar wind for specific energy bands.  $\alpha_{\text{H}}$  represents the parameter for SWCX with the neutral hydrogen, in the unit of eV cm<sup>2</sup>, which is calculated as:

$$\alpha_{\text{H}} = \sigma_{\text{X}^{q+},\text{H}} \cdot Y_{\text{X}^{(q-1)+}} \cdot \left[ \frac{\text{X}^{q+}}{\text{O}} \right] \cdot \left[ \frac{\text{O}}{\text{H}^+} \right] \quad (6)$$

Please find more details about the parameter  $\alpha$  in Koutroumpa (2023).  $n_{\text{H}^+} \cdot v_{\text{H}^+}$  indicates the solar wind proton flux in the MHD simulations. And  $n_{\text{H}}$  indicates the neutral density (only hydrogen is considered here), which can be estimated from a simple exospheric density equation (Cravens et al., 2001), adapted from the Hodges Jr. (1994) model:

$$n_{\text{H}} = 25 \left( \frac{10R_E}{R} \right)^3 (\text{cm}^{-3}), \quad (7)$$

where R indicates the distance from the Earth's center measured in  $R_E$ . The same exospheric neutral hydrogen model is used in the LaTeP approach.

## 2.2. LaTeP Model

The LaTeP model is based on a Monte Carlo approach, in which we launch a large number of test particles (i.e., macro particles representing solar wind ions) and trace their motions under the influence of given magnetic and electric field. The simulation is performed on a cubic uniform grid containing  $400 \times 400 \times 400$  cells. The numerical domain is  $0 \leq X \leq 20 R_E$ ,  $-10 \leq Y \leq 10 R_E$ , and  $-10 \leq Z \leq 10 R_E$  of GSM coordinate system, with the

minimum grid spacing of  $0.05 R_E$  along all directions. A total number of 37.5 million test particles are launched in the simulation box, which is sufficient to obtain statistically robust results, according to the previous applications of the test particle model (Carnielli et al., 2019; Koutroumpa et al., 2012). The particles are launched successively at random positions on the entrance surface (Y-Z plane,  $X = 20R_E$ ) with velocities represented by a Maxwellian distribution applied to all three components ( $V_x$ ,  $V_y$  and  $V_z$ ).

The number of test particles in simulation is far less than the number of physical particles in reality due to the limitation of the computational resources. Each test particle is assigned a weight which is proportional to the number of physical particles, so that the contribution of test particles can be converted to the proportional contribution of hypothetical physical particles. The initial weight  $w_0$  of each injected test particle representing solar wind proton can be calculated as:

$$w_0 = \frac{n_{SW} \cdot v_{SW} \cdot S \cdot \Delta t}{N_{tot}}, \quad (8)$$

where  $n_{SW}$  and  $v_{SW}$  indicate the solar wind density and velocity from the initial ambient solar wind conditions in the MHD models, respectively.  $N_{tot}$  indicates the total number of test particles,  $S$  indicates the surface of the Y-Z injection plane in the simulation and  $\Delta t$  indicates the time step.

After deriving the weight  $w_0$  of a single numerical particle representing solar wind proton, we can then determine the number of physical particles of the species  $X^{q+}$  by simply taking into account their relative abundance with respect to solar wind protons:

$$N_{X^{q+}} = N_{SW} \cdot \left[ \frac{X^{q+}}{O} \right] \cdot \left[ \frac{O}{H^+} \right], \quad (9)$$

where  $N_{SW}$  and  $N_{X^{q+}}$  indicate the number of physical particles representing solar wind proton and  $X^{q+}$ , respectively.

A physical particle will be transformed into a lower charge state ion when it undergoes the charge exchange reaction. The number of produced ions is determined by the number of parent ions lost at a particular position in space and as a function of time, according to the equation:

$$\frac{\partial N_{X^{q+}}}{\partial t} = -N_{X^{q+}} \cdot \sigma_{X^{q+},M} \cdot v_{X^{q+}} \cdot n_M \quad (10)$$

by solving Equation 10, assuming constant speed and neutral component quantity during the time interval ( $t - \Delta t$ ,  $t$ ), the number of parent ions evolves according to:

$$N_{X^{q+}}(t) = N_{X^{q+}}(t - \Delta t) \cdot e^{-\sigma_{X^{q+},M} \cdot v_{X^{q+}} \cdot n_M \cdot \Delta t} \quad (11)$$

therefore, a fraction  $w(t)$  to indicate the test particle transformed during the charge exchange can be written as:

$$w(t) = w(t - \Delta t) \cdot (1 - e^{-\sigma_{X^{q+},M} \cdot v_{X^{q+}} \cdot n_M \cdot \Delta t}) \quad (12)$$

We continually push the test particle until either it exits the simulation box, or it reaches a minimum altitude of  $1 R_E$ , or its numerical weight is  $10^{-6}$  times the original solar wind contribution. The X-ray production of the lower charge state ions  $X^{(q-1)+}$  in an energy range  $\Delta E$  generated by a single numerical test particle in one cell is:

$$q_{X^{(q-1)+}}(t) = \left[ \frac{X^{q+}}{O} \right] \cdot \left[ \frac{O}{H^+} \right] \cdot \sum_{\Delta E} Y_{X^{(q-1)+}} \cdot \frac{w(t)}{\Delta t \cdot \Delta V} \quad (13)$$

where  $\sum_{\Delta E} Y_{X^{(q-1)+}}$  indicates the emission line energy combined all transitions in the energy range  $\Delta E$ ,  $\Delta V$  indicates the volume of the cell.

Each test particle moves with respect to the local electric and magnetic field and at each time step we determine the production of the lower charge state ions, adjust the weight of the test particle and sample its contribution to the X-ray emissions in the corresponding simulation cells. Therefore the X-ray emissions are proportional to the residence of time of the test particle in a given cell. Then by accumulating X-ray emissions generated by all test particles, we can obtain the volume emissivity for a given ion species:

$$Q_{\text{LaTeP}}^{X^{q+}} = \sum_{n=1}^{N_{\text{tot}}} q_{X^{(q-1)+,n}} \quad (14)$$

Note that for simplicity, we keep the species of the parent ion  $X^{q+}$  to refer to the emissions produced by the emitting ions  $X^{(q-1)+}$ .

The total soft X-ray emissions calculated in the LaTeP model is a sum of different ion species emissions:

$$Q_{\text{LaTeP}} = \sum_{X^{q+}} Q_{\text{LaTeP}}^{X^{q+}} = Q_{\text{LaTeP}}^{O^{7+}} + Q_{\text{LaTeP}}^{O^{8+}} + \dots \quad (15)$$

Each ion species is characterized by different abundance and cross-section with neutral hydrogen. Therefore, it is possible to compare the impact of different ion species and to investigate the individual spectral characteristics.

Normally, to get the global X-ray emission generated by test particles, it requires us to continuously launch test particles until the simulation box is fully filled. Since the magnetic and electric field will not change during the simulation, we launch each randomly generated test particle only once, and assume that its trajectory is representative of all the particles launched with the same initial conditions. The accumulated X-ray emissions produced along this trajectory will then represent the emission contribution of the past, present and future test particles that follow the same trajectory. This way the results derived from LaTeP model can be considered as the steady state results. Koutroumpa et al. (2012) provides more details about the LaTeP model.

### 3. Results

#### 3.1. Emissions From Pure MHD Approach

The emissivity map from pure MHD approach can be derived based on Equation 5. To compare with the LaTeP results of  $O^{7+}$ , the value of  $\alpha_H$  is set to be  $1.84 \times 10^{-16}$  eV cm<sup>2</sup> here to calculate the emissions of  $O^{7+}$  over the full energy range of the SXI instrument (0.2–2 keV) (Sembay et al., 2023). The volume emissivity of  $O^{7+}$  from pure OpenGGCM and PPMLR MHD models are presented in Figure 1. To indicate the general location of the magnetopause, we take the predictions of Shue et al. (1998) model under the solar wind conditions listed in Table 1 as a reference, exhibited as the dashed line in the figure. In reality, the soft X-ray emission in the magnetosphere is fairly weak. However, as mentioned before, the MHD model cannot distinguish between the solar wind plasma and magnetospheric plasma, and the MHD model may predict the density inside the magnetosphere to be higher than the observation. According to Equation 5, the emissions from pure MHD approach is influenced by plasma density including both solar wind and magnetospheric plasma, where as only solar wind plasma is capable of generating SWCX X-ray emission. This will cause the soft X-ray emissions inside the magnetosphere to be stronger than it should be (Figures 1a, 1b, and 1d), thus a masking method (e.g., using threshold conditions (Samsonov, Carter, et al., 2022)) is needed to cover the plasma inside the magnetosphere when deriving X-ray emissions from pure MHD approach.

There is a clear boundary of X-ray emissions between the magnetosphere and magnetosheath in both OpenGGCM and PPMLR results. We take this boundary as the location of magnetopause revealed by X-ray emissions from pure MHD approach. The width of the subsolar magnetosheath in OpenGGCM results is approximately  $2.7 R_E$  and is larger than that in PPMLR results ( $\sim 2.2 R_E$ ). The cusps region revealed in OpenGGCM results seems thinner and smoother than in the PPMLR results, although this is probably an effect of indissociable plasma in the magnetosphere in the PPMLR model that artificially enhances the emission. We note that in OpenGGCM results, the X-ray emission at the dayside magnetopause is generally stronger than that in PPMLR results. This is mainly due to the fact that the density of geocorona neutral hydrogen falls as  $1/R^3$ , and that

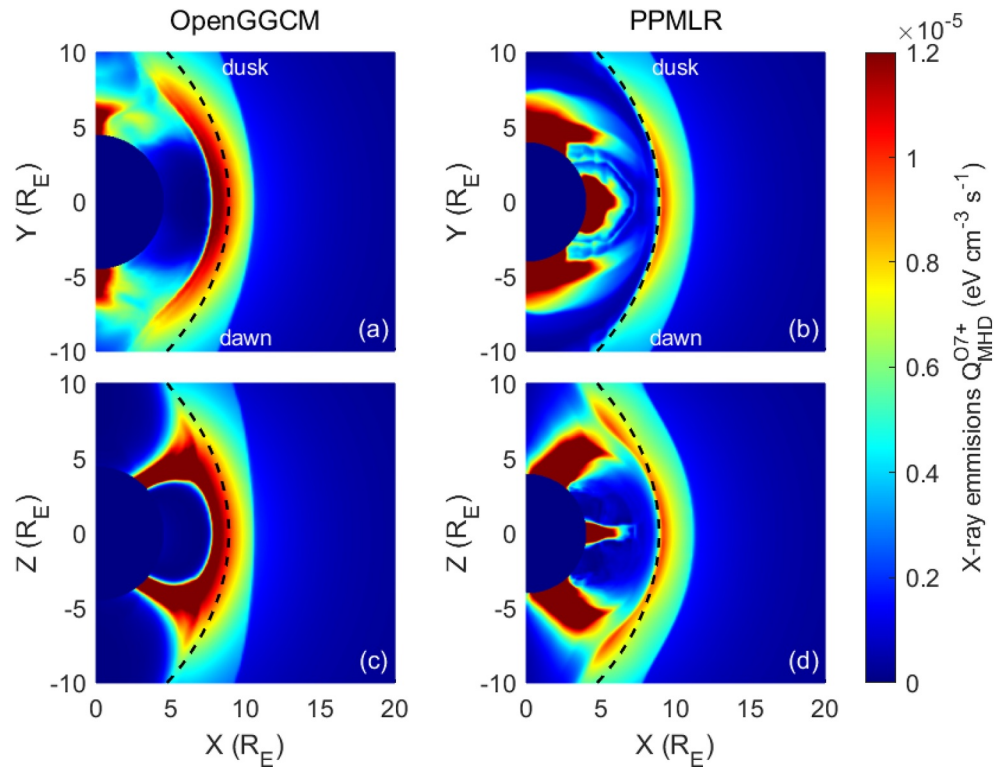


**Figure 1.** The soft X-ray volume emissivity of  $O^{7+}$  in the equatorial (a and b) and noon-midnight meridian (c and d) plane from pure MHD approach (a and c) and (b and d) indicate the results of OpenGGCM and PPMLR MHD models, respectively. The dotted black lines indicate the predictions from the empirical magnetopause model (Shue et al., 1998). The blue circles indicate the inner boundary of MHD simulations.

the subsolar magnetopause in OpenGGCM results ( $7.8 R_E$ ) is more Earthward than in the PPMLR results ( $8.9 R_E$ ), resulting in smaller neutral hydrogen density at the magnetopause in PPMLR results.

By comparing the emission results of pure MHD approach (Figure 1) with the electro-magnetic field, density, velocity and pressure in MHD models (Figures S1–S5 in Supporting Information S1), we can see that the pure MHD approach results are consistent with the density, velocity and pressure in MHD models. This consistency is supported by Equation 5, as the emissions of pure MHD approach are calculated from density and velocity. Therefore, the differences between pure OpenGGCM and pure PPMLR emission results come from the differences between physical quantities (e.g., velocity, density, pressure) in these two MHD models. A more detailed comparison of the two MHD models is beyond the scope of this paper.

To conclude, the MHD models are capable of simulating soft X-ray emission at the dayside magnetopause. However, there are still several limitations in the MHD model, such as the MHD model cannot resolve particle kinetic effects and usually requires a masking method to separate the magnetosphere from the magnetosheath. To address these limitations, we then perform simulations based on the LaTeP model to derive the soft X-ray emissions near the magnetopause.

### 3.2. Emissions of $O^{7+}$ From LaTeP-MHD Approach

We use the magnetic and electric field data derived from OpenGGCM and PPMLR MHD models as the input of the LaTeP model to simulate the X-ray emissions. The simulation results of the volume emissivity of  $O^{7+}$  from LaTeP-OpenGGCM and LaTeP-PPMLR approaches are presented in Figure 2. The emissivity maps for other ion species exhibit very similar trends with the  $O^{7+}$  maps. The maps for ion species:  $C^{5+}$ ,  $C^{6+}$ ,  $N^{6+}$ ,  $N^{7+}$ ,  $O^{8+}$ ,  $Ne^{9+}$ ,  $Mg^{10+}$ , and  $Mg^{11+}$  are provided in the Supporting Information. Note that the emissions for each ion species here contain the emission line for the full energy range of the SXI instrument. Unlike the pure MHD approach results, there is no confusion between the solar wind and magnetospheric plasma in the LaTeP-MHD approach. This is



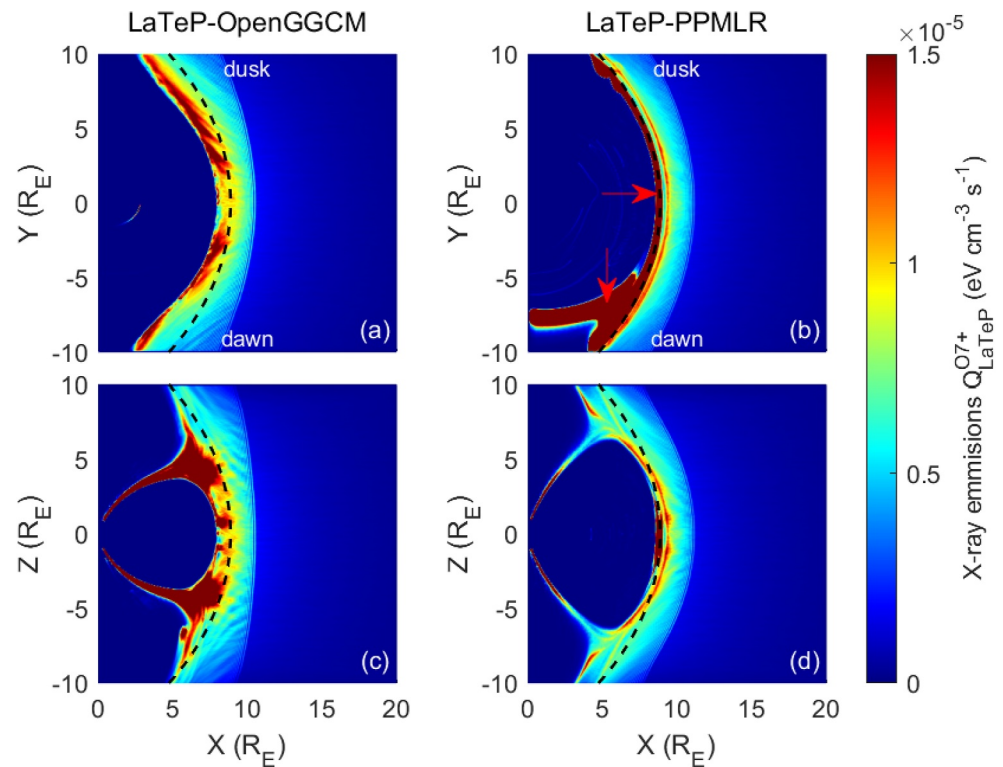


**Figure 2.** The soft X-ray volume emissivity of  $O^{7+}$  in the equatorial (a and b) and noon-midnight meridian (c and d) plane from LaTeP-MHD approach (a and c) and (b and d) indicate the results of LaTeP-OpenGGCM and LaTeP-PPMLR models, respectively. The dotted black lines indicate the predictions from the empirical magnetopause model (Shue et al., 1998). The red arrows indicate the regions where the emissions are unusually strong.

because the LaTeP model simulates the motion of the particles launched in the solar wind, thus the particles are usually unable to enter the closed field lines in the magnetosphere, resulting in weak or no emission inside the magnetosphere. Therefore, it is not necessary to use a masking method in the LaTeP-MHD approach results. The LaTeP model allows us to clearly define the magnetopause location in the emissivity profiles.

In Figure 2, the magnetopause, bow shock and cusp regions are clearly displayed. Regarding the magnetopause location, the LaTeP-MHD approach yields consistent results with the pure MHD approach. Similarly, the magnetopause location in LaTeP-OpenGGCM approach (Figures 2a and 2c) is more Earthward than the LaTeP-PPMLR results (Figures 2b and 2d). However, regarding the cusps region, the cusps revealed in the LaTeP-MHD approach are much thinner and more obvious than in the pure MHD approach, especially in the PPMLR case where artificially strong emission from magnetospheric plasma conceals the cusp emission.

Another difference is that the LaTeP-MHD approach exhibits many small scale structures that the emission changes considerably along the magnetosheath. For instance, we can see the streamlines of particle motions in response to the electro-magnetic field input. In this case, small scale variation in the electric field  $E_y$  component influenced the dynamic of test particles, leading to these streamline structures in emissivity.

There are also differences between LaTeP-OpenGGCM and LaTeP-PPMLR results. The emissions in the cusps region in LaTeP-OpenGGCM results (Figure 2c) is much stronger and spatially broader than that in LaTeP-PPMLR results (Figure 2d). By comparing the emission results of LaTeP-MHD approach (Figure 2) with the electro-magnetic field data (Figures S1 and S2 in Supporting Information S1), it is clear that the emissions produced by test particles in LaTeP model are regulated by the configuration of electro-magnetic field data. The location of magnetopause, bow shock and cusps revealed in LaTeP-MHD results all correspond well to the electro-magnetic field configurations, indicating the consistency between MHD model and LaTeP model. To conclude, the differences between physical quantities in OpenGGCM and PPMLR models lead to different behaviors of test particles, eventually resulting in different emissions in LaTeP-OpenGGCM and LaTeP-PPMLR.

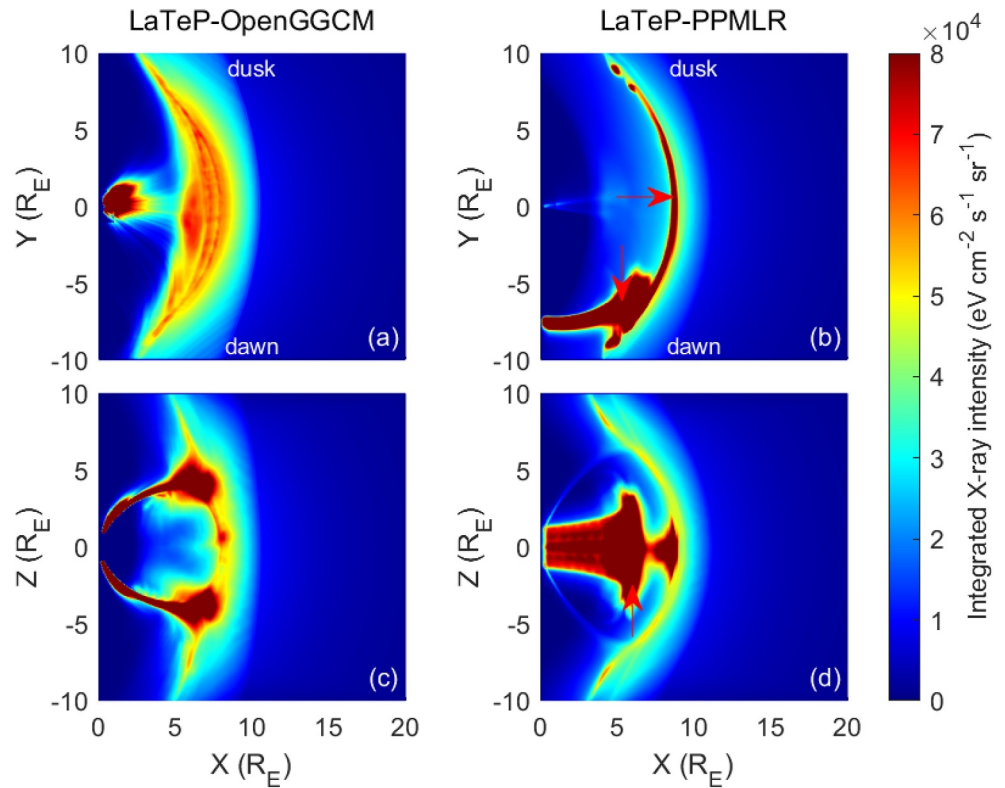


**Figure 3.** X-ray intensity integrated along main axes for LaTeP-OpenGGCM (a and c) and LaTeP-PPMLR (b and d) approaches (a and b) and (c and d) indicate the results integrated along z and y axis, respectively. The red arrows indicate the regions where the emissions are unusually strong.

One may notice that as pointed by the red arrows in Figure 2b, the emissions are unusually strong within the region slightly inside the dotted line and the flank magnetopause (in the region  $Y \sim -7 R_E$ ). Part of these strong emissions is actually produced by the particles trapped inside the magnetosphere, which we will discuss in detail in Section 4.

By comparing the results of the pure MHD approach and LaTeP-MHD approach, we can see that under the same initial solar wind conditions, there are still differences between LaTeP-MHD approach and pure MHD approach, as well as between PPMLR and OpenGGCM results. Also, there are several unique advantages that LaTeP model has. Firstly, the LaTeP-MHD approach introduces kinetic effects due to the ion gyromotion. This will allow us to distinguish small scale structures, such as oscillations downstream of the bow shock associated to the gyro motion also referred as the bow shock overshoot (Lowe & Burgess, 2003). Secondly, the MHD models are based on single-fluid simulations that cannot distinguish solar wind from magnetospheric plasma, therefore some inner regions of the simulated magnetosphere have to be artificially masked in order to reveal the magnetosheath SWCX emission. The LaTeP-MHD approach allows a clean view of the SWCX emission.

### 3.3. Global Intensity Maps From the LaTeP-MHD Approach

For the X-ray intensity maps integrated along the line of sight in the LaTeP model, it is generally the sum of the X-ray emissions of all the ion species mentioned above:

$$I_{\text{LaTeP}} = \frac{1}{4\pi} \int \sum_{\text{X}^{q+}} Q_{\text{LaTeP}}^{\text{X}^{q+}}(\vec{r}) \cdot ds \quad (16)$$

Figure 3 indicates the X-ray intensity integrated along z and y axis in the LaTeP-MHD approach. By comparing the intensity map integrated along z axis in Figures 3a and 3b, there exists a broad region showing strong intensity in the LaTeP-OpenGGCM results, whereas in the LaTeP-PPMLR results the intensity is relatively low between

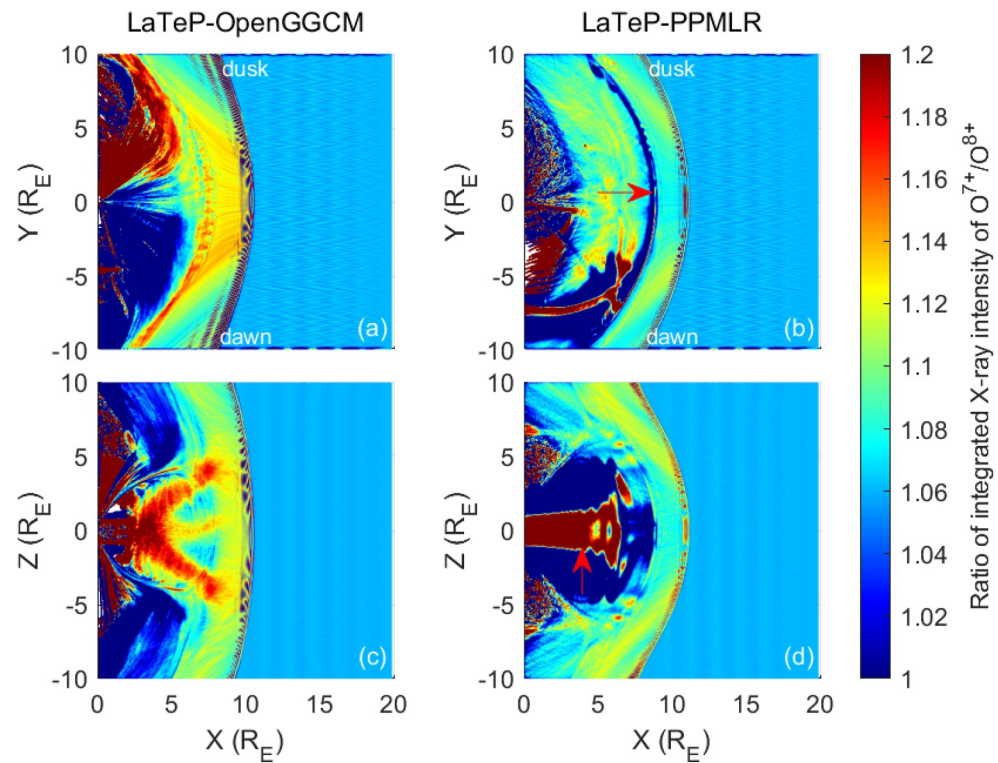


**Figure 4.** The ratio between the OVII (0.57 keV) and OVIII (0.65 keV) spectral line maps in the equatorial (a and b) and noon-midnight meridian (c and d) plane from LaTeP-MHD approach (a and c) and (b and d) indicate the results of LaTeP-OpenGGCM and LaTeP-PPMLR models, respectively. The red arrows indicate the regions where the emissions are unusually strong.

the range of 5–8  $R_E$ . The broad region with strong intensity is produced because we integrate through the beginning of the cusp region (along  $X \sim 5 R_E$  in Figures 2c and 2d), which is broader and enhanced in the LaTeP-OpenGGCM compared to LaTeP-PPMLR. In LaTeP-OpenGGCM X-Y projection the magnetopause location is harder to derive due to the enhanced contribution from the cusps. In the intensity map integrated along the y axis, the intensity near the cusps region is prominent in the LaTeP-OpenGGCM results (Figure 3c) and is much stronger than in the LaTeP-PPMLR results (Figure 3d). As pointed by the red arrows, the LaTeP-PPMLR maps are generally dominated by the emission produced by test-particles trapped in the magnetosphere.

### 3.4. OVII/OVIII Spectral Line Ratio Maps

To investigate the spectral characteristics of different ion species and to compare observables that can be easily extracted from processed SXI spectra, we compare the ratio of integrated X-ray maps from the OVII triplet (produced by charge exchange of  $O^{7+}$  at  $\sim 0.57$  keV) and the OVIII Ly-alpha line (produced by charge exchange of  $O^{8+}$  at 0.65 keV), namely the ratio of  $O^{7+}$  to  $O^{8+}$  maps (Figure 4). Generally, the OVII triplet emission is stronger than the OVIII line, which is due to the abundance of  $O^{7+}$  ions in the solar wind being higher than the abundance of  $O^{8+}$ . Also the emission probability for the OVII triplet is also higher than the one for the OVIII line. The ratio is  $\sim 1.05$ , 1.20, and 1.10 in the solar wind, bow shock and magnetosheath, respectively. In the LaTeP-OpenGGCM results, this ratio exhibits an asymmetry inside the magnetopause as shown in Figure 4a, which is attributed to the different emissions of  $O^{7+}$  and  $O^{8+}$  in the magnetosphere. The emissions in the magnetosphere is considered to be very low, therefore such asymmetry is not revealed in the integrated X-ray intensity map. And there is a tilted V-shaped structure in Figure 4c that resembles the cusps region. However, this structure is actually located at the flank magnetopause and only appears to align with the cusps region due to integration. In the LaTeP-PPMLR results, there is a curved region near the magnetopause where the ratio decreases sharply as shown in Figure 4b, and a region near the equatorial plane where the ratio is unusually high as shown in Figure 4d

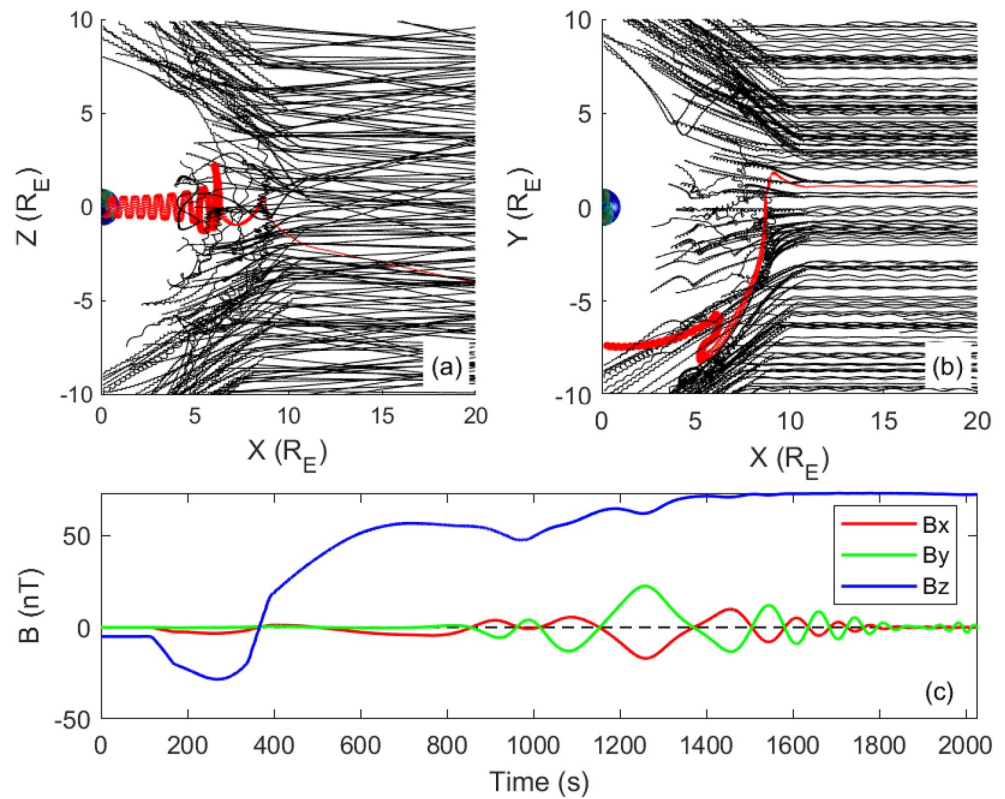


**Figure 5.** (a and b) The trajectories of the test particles. The black and red lines indicate the trajectory of normal and trapped particles, respectively. (c) The magnetic field along the trajectory of the trapped particle versus the time of life of the trapped particle. The red green and blue lines indicate  $B_x$ ,  $B_y$  and  $B_z$ , respectively.

(pointed by the red arrows). These two regions correspond to the unusually strong emission in Figure 2b and is also due to the particles trapped in the magnetosphere, which we will discuss in Section 4.

The X-ray intensity gradient for the bow shock in the projected intensity maps (Figure 3) is not strong enough to clearly define the bow shock location. However, in all subfigures of Figure 4, there is a region where the values are higher compared to the surrounding areas, indicating the location of the bow shock. This outlined bow shock in the OVII/OVIII ratio map is due to the different Larmor radius of  $O^{7+}$  and  $O^{8+}$  (due to their different  $q/m$  ratio) during their gyromotion.

The OVII/OVIII Spectral line ratio maps reveals a distinguished boundary at the bow shock, suggesting that this ratio can be a parameter to identify the bow shock. This may provide us more insights into locating the bow shock through X-ray observations from spacecrafts such as SMILE. Note that this simulation is based on a pure steady state configuration of the magnetosphere and thus temporal variations of the bow shock might blur or attenuated this effect.

#### 4. Discussion and Future Work

We note that in the LaTeP-PPMLR approach, there is an abnormal region where the emission is extremely strong near the flank magnetopause as shown in Figures 2b, 3b, and 3d. To locate the source of the abnormally strong emission, we check the trajectories of the test particles in the simulation box. According to the trajectories of the launched particles (Figures 5a and 5b), in the strong emission region at the dawn side magnetopause, there are a few particles bounce around the equatorial plane and seem to be “trapped.” Based on this result, we can conclude three main factors that contribute to this strong emission: Firstly, in the LaTeP model, we trace the motion of the launched particles, and accumulate the X-ray emissions generated along the trajectories to represent the emission contribution of all particles traveling along the same trajectory in the past, present and future. Secondly, if a few particles get trapped, they will continuously move without leaving the simulation box, having a very long time of

life. Thirdly, the neutral density in the magnetosphere is relatively high, which can also enhance the emission. It should be remembered that only a small fraction of the launched particles charge exchange within the simulation box. However, particles on “trapped” trajectories must charge exchange completely because they have a long time of life traveling in a high neutral density region, thus producing strong emission. The unphysical situation is artificially caused by the way we accumulate the contribution along the trajectories, which is simple, but approximate. This approximation breaks down when a large fraction of the particles charge exchange. And note that the trapped particles are not unique to PPMLR, but has been seen in other OpenGGCM runs (not shown in this study).

Figure 5c indicates the magnetic field along the trajectory of one trapped particle. This trapped particle enters the magnetopause at  $\sim 400$  s and then bounces in the Earth's magnetic field, which is unusual since normally the particles should move along the magnetopause instead of entering the magnetosphere. This transport of solar wind ions into the magnetosphere is probably due to the Kelvin-Helmholtz instability or the reconnection at dayside magnetopause (Lu et al., 2013; Sorathia et al., 2019; Yan et al., 2009).

Accumulating the contribution along the trajectories is an approximate and simple method to obtain the emission map. However, this approximation raises certain issues such as the unusually strong emission from the trapped particles. To address this issue, it is necessary to develop an improved model that can obtain the global distribution of all the particles and calculate the emissions of each particle individually, instead of using the approximation method mentioned above.

The magnetic and electric fields remain unchanged once loaded during the simulation, resulting in the current LaTeP model only being able to adapt to a quasi-steady magnetosphere and obtain quasi-steady results. During the simulation, the time of life of the particles that are not trapped is typically  $\sim 8$  min. However, the solar wind conditions are highly dynamical in reality, implying that the solar wind conditions may undergo significant changes within this 8-min period. The current LaTeP model cannot well resolve the situation of time-varying solar wind conditions. There is a feasible solution being used in the LatHyS model (Aizawa et al., 2022; Modolo et al., 2018), based on which an improved LaTeP model is currently under development for better processing the time-dependent magnetic and electric field.

## 5. Conclusion

The LaTeP model does not self compute the magnetic field and electric field, while MHD model can. We use the magnetic and electric field data obtained from OpenGGCM and PPMLR MHD model as the input to LaTeP model. The soft X-ray emissions simulated from pure OpenGGCM and PPMLR MHD approaches and from LaTeP-OpenGGCM and LaTeP-PPMLR approaches are presented and compared. The results give an average range of expected X-ray emissivities and signatures under southward IMF conditions. The results indicate that there are certain advantages that LaTeP model introduces. Firstly, the LaTeP model introduces kinetic effects due to the ion gyromotion, and therefore exhibits many small scale structures. Secondly, the MHD model adapts single-fluid description, thus cannot distinguish between the solar wind and magnetospheric plasma. In the LaTeP model, the solar wind ions are treated as particles, allowing us to conduct simulations for individual ion species, enabling a more detailed analysis of spectral characteristics of different ion species. And there is no confusion between the solar wind and magnetospheric plasma in the LaTeP model, thus can provide a clear perspective on the SWCX emission near the magnetopause and the cusps region. Therefore, the LaTeP model is a novel approach for simulating the X-ray emissions. By investigating the ratio of the integrated X-ray intensity of  $O^{7+}/O^{8+}$ , we find this ratio relatively higher at the bow shock than the surrounding areas, suggesting it may be an effective parameter to identify the location of the bow shock. This paper combines the advantages of both LaTeP and MHD models and can help on the interpretation of X-ray observations.

## Data Availability Statement

Simulation results are available through the interactive catalogue <http://impex.latos.ipsl.fr/LatHyS.htm>. The simulation data used in the manuscript correspond to simulation ID LaTeP\_PPMLR\_15\_02\_24 and LaTeP\_OpenGGCM\_15\_02\_24.

**Acknowledgments**

This work was supported by CNES, through the Soleil-Heliosphere-Magnetosphere program and partially supported by the National Key R&D Program of China (2021YFA0718600). This study benefited from the IPSL Data and Computing Center ESPRI which is supported by CNRS, SU, CNES and Ecole Polytechnique and ANR TEMPETE project. Q. Xu is funded by the CSC-Université Paris-Saclay Grant 202204910154. And we wish to warmly thank the two anonymous referees for their thorough evaluation and valuable suggestions that greatly improved the quality of the manuscript.

**References**

Aizawa, S., Persson, M., Menez, T., André, N., Modolo, R., Génot, V., et al. (2022). Lathys global hybrid simulation of the bepicolombo second Venus flyby. *Planetary and Space Science*, 218, 105499. <https://doi.org/10.1016/j.pss.2022.105499>

Branduardi-Raymont, G., Wang, C., Escoubet, C. P., Adamovic, M., Agnolon, D., Berthomier, M., et al. (2018). *Smile definition study report (V1.0 ed.; Tech. Rep.)*. ESA/SCI. <https://doi.org/10.5270/esa.smile.definition.study.report-2018-12>

Cahill, L. J., & Amazeen, P. G. (1963). The boundary of the geomagnetic field. *Journal of Geophysical Research (1896–1977)*, 68(7), 1835–1843. <https://doi.org/10.1029/JZ068i007p01835>

Carnielli, G., Galand, M., Leblanc, F., Leclercq, L., Modolo, R., Beth, A., et al. (2019). First 3d test particle model of Ganymede's ionosphere. *Icarus*, 330, 42–59. <https://doi.org/10.1016/j.icarus.2019.04.016>

Carter, J. A., Sembay, S., & Read, A. M. (2010). A high charge state coronal mass ejection seen through solar wind charge exchange emission as detected by XMM–Newton. *Monthly Notices of the Royal Astronomical Society*, 402(2), 867–878. <https://doi.org/10.1111/j.1365-2966.2009.15985.x>

Colella, P., & Woodward, P. R. (1984). The Piecewise Parabolic Method (PPM) for gas-dynamical simulations. *Journal of Computational Physics*, 54(1), 174–201. [https://doi.org/10.1016/0021-9991\(84\)90143-8](https://doi.org/10.1016/0021-9991(84)90143-8)

Collier, M. R., & Connor, H. K. (2018). Magnetopause surface reconstruction from tangent vector observations. *Journal of Geophysical Research: Space Physics*, 123(12), 10189–10199. <https://doi.org/10.1029/2018JA025763>

Collier, M. R., Snowden, S. L., Sarantos, M., Benna, M., Carter, J. A., Cravens, T. E., et al. (2014). On lunar exospheric column densities and solar wind access beyond the terminator from rosat soft x-ray observations of solar wind charge exchange. *Journal of Geophysical Research: Planets*, 119(7), 1459–1478. <https://doi.org/10.1002/2014JE004628>

Connor, H. K., Sibeck, D. G., Collier, M. R., Baliukin, I. I., Branduardi-Raymont, G., Brandt, P. C., et al. (2021). Soft X-ray and Ena imaging of the Earth's dayside magnetosphere. *Journal of Geophysical Research: Space Physics*, 126(3), e2020JA028816. <https://doi.org/10.1029/2020JA028816>

Cravens, T. E., Robertson, I. P., & Snowden, S. L. (2001). Temporal variations of geocoronal and heliospheric X-ray emission associated with the solar wind interaction with neutrals. *Journal of Geophysical Research*, 106(A11), 24883–24892. <https://doi.org/10.1029/2000JA000461>

Cucho-Padin, G., Connor, H., Jung, J., Walsh, B., & Sibeck, D. G. (2023). Finding the magnetopause location using soft X-ray observations and a statistical inverse method. *Earth and Planetary Physics*, 8(1), 184–203. <https://doi.org/10.26464/epp2023070>

Cumbee, R., Stancil, P., & McIlvane, S. (2021). The interactive kronos charge exchange database. *Bulletin of the AAS*, 53(6).

Dennerl, K. (2008). X-Rays from Venus observed with Chandra. *Planetary and Space Science*, 56(10), 1414–1423. <https://doi.org/10.1016/j.pss.2008.03.008>

Dunn, W. R., Weigt, D. M., Grodent, D., Yao, Z. H., May, D., Feigelman, K., et al. (2022). Jupiter's X-ray and UV dark polar region. *Geophysical Research Letters*, 49(11), e2021GL097390. <https://doi.org/10.1029/2021GL097390>

Fujimoto, R., Mitsuda, K., McCammon, D., Takei, Y., Bauer, M., Ishisaki, Y., et al. (2007). Evidence for solar-wind charge-exchange X-ray emission from the Earth's magnetosheath. *Publications of the Astronomical Society of Japan*, 59(sp1), S133–S140. <https://doi.org/10.1093/pasj/59.sp1.S133>

Grandin, M., Connor, H. K., Hoilijoki, S., Battarbee, M., Pfau-Kempf, Y., Ganse, U., et al. (2023). Hybrid-vlasov simulation of soft X-ray emissions at the Earth's dayside magnetospheric boundaries. *Earth and Planetary Physics*, 8(1), 70–88. <https://doi.org/10.26464/epp2023052>

Guo, J., Sun, T., Lu, S., Lu, Q., Lin, Y., Wang, X., et al. (2023). Global hybrid simulations of soft X-ray emissions in the Earth's magnetosheath. *Earth and Planetary Physics*, 8(1), 47–58. <https://doi.org/10.26464/epp2023053>

Guo, Y., Sun, T., Wang, C., & Sembay, S. (2022). Deriving the magnetopause position from wide field-of-view soft X-ray imager simulation. *Science China Earth Sciences*, 65(8), 1601–1611. <https://doi.org/10.1007/s11430-021-9937-y>

Haaland, S., Runov, A., Artemyev, A., & Angelopoulos, V. (2019). Characteristics of the flank magnetopause: Themis observations. *Journal of Geophysical Research: Space Physics*, 124(5), 3421–3435. <https://doi.org/10.1029/2019JA026459>

Hodges, R. R., Jr. (1994). Monte Carlo simulation of the terrestrial hydrogen exosphere. *Journal of Geophysical Research*, 99(A12), 23229–23247. <https://doi.org/10.1029/94JA02183>

Hu, Y. Q., Guo, X. C., & Wang, C. (2007). On the ionospheric and reconnection potentials of the Earth: Results from global MHD simulations. *Journal of Geophysical Research*, 112(A7), A07215. <https://doi.org/10.1029/2006JA012145>

Ishikawa, K., Ezoe, Y., Miyoshi, Y., Terada, N., Mitsuda, K., & Ohashi, T. (2013). Suzaku observation of strong solar-wind charge-exchange emission from the terrestrial exosphere during a geomagnetic storm. *Publications of the Astronomical Society of Japan*, 65(3), 63. <https://doi.org/10.1093/pasj/65.3.63>

Kharchenko, V. (2005). Charge-exchange mechanism of X-ray emission. *AIP Conference Proceedings*, 774(1), 271–280. <https://doi.org/10.1063/1.1960938>

Kharchenko, V., & Dalgarno, A. (2000). Spectra of cometary X rays induced by solar wind ions. *Journal of Geophysical Research*, 105(A8), 18351–18359. <https://doi.org/10.1029/1999JA000203>

Kim, H., Connor, H. K., Jung, J., Walsh, B. M., Sibeck, D., Kuntz, K. D., et al. (2023). Estimating the subsolar magnetopause position from soft X-ray images using a low-pass image filter. *Earth and Planetary Physics*, 8(1), 173–183. <https://doi.org/10.26464/epp2023069>

Koutroumpa, D. (2023). Solar wind ion charge state distributions and compound cross sections for solar wind charge exchange X-ray emission. *Earth and Planetary Physics*, 8(1), 105–118. <https://doi.org/10.26464/epp2023056>

Koutroumpa, D., Lallement, R., Kharchenko, V., Dalgarno, A., Pepino, R., Izmodenov, V., & Quémerais, E. (2006). Charge-transfer induced EUV and soft X-ray emissions in the heliosphere. *Astronomy & Astrophysics*, 460(1), 289–300. <https://doi.org/10.1051/0004-6361/20065250>

Koutroumpa, D., Modolo, R., Chanteur, G., Chaufray, J.-Y., Kharchenko, V., & Lallement, R. (2012). Solar wind charge exchange X-ray emission from Mars—Model and data comparison. *Astronomy & Astrophysics*, 545, A153. <https://doi.org/10.1051/0004-6361/201219720>

Kuntz, K. D., Collado-Vega, Y. M., Collier, M. R., Connor, H. K., Cravens, T. E., Koutroumpa, D., et al. (2015). The solar wind charge-exchange production factor for hydrogen. *The Astrophysical Journal*, 808(2), 143. <https://doi.org/10.1088/0004-637X/808/2/143>

Liang, G. Y., Sun, T. R., Lu, H. Y., Zhu, X. L., Wu, Y., Li, S. B., et al. (2023). X-ray morphology due to charge-exchange emissions used to study the global structure around Mars. *The Astrophysical Journal*, 943(2), 85. <https://doi.org/10.3847/1538-4357/acac7e>

Lisse, C. M., Dennerl, K., Englhauser, J., Harden, M., Marshall, F. E., Mumma, M. J., et al. (1996). Discovery of X-ray and extreme ultraviolet emission from comet c/hyakutake 1996 b2. *Science*, 274(5285), 205–209. <https://doi.org/10.1126/science.274.5285.205>

Lowe, R. E., & Burgess, D. (2003). The properties and causes of rippling in quasi-perpendicular collisionless shock fronts. *Annales Geophysicae*, 21(3), 671–679. <https://doi.org/10.5194/angeo-21-671-2003>

Lu, J. Y., Jing, H., Liu, Z. Q., Kabin, K., & Jiang, Y. (2013). Energy transfer across the magnetopause for northward and southward interplanetary magnetic fields. *Journal of Geophysical Research: Space Physics*, 118(5), 2021–2033. <https://doi.org/10.1002/jgra.50093>

- Modolo, R., Hess, S., Génot, V., Leclercq, L., Leblanc, F., Chaufray, J. Y., et al. (2018). The lathys database for planetary plasma environment investigations: Overview and a case study of data/model comparisons. *Planetary and Space Science*, *150*, 13–21. <https://doi.org/10.1016/j.pss.2017.02.015>
- Mullen, P. D., Cumbee, R. S., Lyons, D., Gu, L., Kaastra, J., Shelton, R. L., & Stancil, P. C. (2017). Line ratios for solar wind charge exchange with comets. *The Astrophysical Journal*, *844*(1), 7. <https://doi.org/10.3847/1538-4357/aa7752>
- Ng, J., Walsh, B. M., Chen, L.-J., & Omelchenko, Y. (2023). Soft x-ray imaging of Earth's dayside magnetosheath and cusps using hybrid simulations. *Geophysical Research Letters*, *50*(10), e2023GL103347. <https://doi.org/10.1029/2023GL103347>
- Raeder, J., Larson, D., Li, W., Kepko, E. L., & Fuller-Rowell, T. (2008). Openggem simulations for the Themis mission. *Space Science Reviews*, *141*(1), 535–555. <https://doi.org/10.1007/s11214-008-9421-5>
- Robertson, I. P., Collier, M. R., Cravens, T. E., & Fok, M.-C. (2006). X-ray emission from the terrestrial magnetosheath including the cusps. *Journal of Geophysical Research*, *111*(A12), A12105. <https://doi.org/10.1029/2006JA011672>
- Robertson, I. P., & Cravens, T. E. (2003). X-ray emission from the terrestrial magnetosheath. *Geophysical Research Letters*, *30*(8), 1439. <https://doi.org/10.1029/2002GL016740>
- Samsonov, A., Bogdanova, Y. V., Branduardi-Raymont, G., Xu, L., Zhang, J., Sormakov, D., et al. (2021). Geosynchronous magnetopause crossings and their relationships with magnetic storms and substorms. *Space Weather*, *19*(6), e2020SW002704. <https://doi.org/10.1029/2020SW002704>
- Samsonov, A., Carter, J. A., Read, A., Sembay, S., Branduardi-Raymont, G., Sibeck, D., et al. (2022a). Finding magnetopause standoff distance using a soft X-ray imager: 1. Magnetospheric masking. *Journal of Geophysical Research: Space Physics*, *127*(12), e2022JA030848. <https://doi.org/10.1029/2022JA030848>
- Samsonov, A., Sembay, S., Read, A., Carter, J. A., Branduardi-Raymont, G., Sibeck, D., et al. (2022b). Finding magnetopause standoff distance using a soft X-ray imager: 2. Methods to analyze 2-d X-ray images. *Journal of Geophysical Research: Space Physics*, *127*(12), e2022JA030850. <https://doi.org/10.1029/2022JA030850>
- Sembay, S., Alme, A. L., Agnolon, D., Arnold, T., Beardmore, A., Margeli, A. B. B., et al. (2023). The Soft X-ray Imager (SXI) on the smile mission. *Earth and Planetary Physics*, *8*(1), 5–14. <https://doi.org/10.26464/epp2023067>
- Shue, J.-H., Song, P., Russell, C. T., Steinberg, J. T., Chao, J. K., Zastenker, G., et al. (1998). Magnetopause location under extreme solar wind conditions. *Journal of Geophysical Research*, *103*(A8), 17691–17700. <https://doi.org/10.1029/98JA01103>
- Sibeck, D. G., Allen, R., Aryan, H., Bodewits, D., Brandt, P., Branduardi-Raymont, G., et al. (2018). Imaging plasma density structures in the soft X-rays generated by solar wind charge exchange with neutrals. *Space Science Reviews*, *214*(4), 79. <https://doi.org/10.1007/s11214-018-0504-7>
- Sorathia, K. A., Merkin, V. G., Ukhorskiy, A. Y., Allen, R. C., Nykyri, K., & Wing, S. (2019). Solar wind ion entry into the magnetosphere during northward IMF. *Journal of Geophysical Research: Space Physics*, *124*(7), 5461–5481. <https://doi.org/10.1029/2019JA026728>
- Sun, T., Wang, C., Connor, H. K., Jorgensen, A. M., & Sembay, S. (2020). Deriving the magnetopause position from the soft X-ray image by using the tangent fitting approach. *Journal of Geophysical Research: Space Physics*, *125*(9), e2020JA028169. <https://doi.org/10.1029/2020JA028169>
- Sun, T., Wang, C., Sembay, S. F., Lopez, R. E., Escoubet, C. P., Branduardi-Raymont, G., et al. (2019). Soft X-ray imaging of the magnetosheath and cusps under different solar wind conditions: MHD simulations. *Journal of Geophysical Research: Space Physics*, *124*(4), 2435–2450. <https://doi.org/10.1029/2018JA026093>
- Tkachenko, Y., Koutroumpa, D., Modolo, R., Connor, H., & Sembay, S. (2021). Charge exchange X-ray emission in the near-Earth environment: Simulations in preparation for the smile magnetospheric mission. In *Sf2a-2021: Proceedings of the annual meeting of the French society of astronomy and astrophysics*. SFA, 487.
- Trattner, K. J., Burch, J. L., Fuselier, S. A., Petrinc, S. M., & Vines, S. K. (2020). The 18 November 2015 magnetopause crossing: The gem dayside kinetic challenge event observed by mms/hpca. *Journal of Geophysical Research: Space Physics*, *125*(7), e2019JA027617. <https://doi.org/10.1029/2019JA027617>
- Walsh, B. M., Collier, M. R., Kuntz, K. D., Porter, F. S., Sibeck, D. G., Snowden, S. L., et al. (2016). Wide field-of-view soft X-ray imaging for solar wind-magnetosphere interactions. *Journal of Geophysical Research: Space Physics*, *121*(4), 3353–3361. <https://doi.org/10.1002/2016JA022348>
- Wang, C., & Branduardi-Raymont, G. (2018). Progress of solar wind magnetosphere ionosphere link explorer (smile) mission. *Chinese Journal of Space Science*, *38*(5), 657–661. <https://doi.org/10.11728/cjss2018.05.657>
- Wedlund, C. S., Behar, E., Nilsson, H., Alho, M., Kallio, E., Gunell, H., et al. (2020). Solar wind charge exchange in cometary atmospheres—III. Results from the Rosetta mission to comet 67p/churyumov-gerasimenko (corrigendum). *Astronomy & Astrophysics*, *640*, A37. <https://doi.org/10.1051/0004-6361/201834881e>
- Whittaker, I. C., Sembay, S., Carter, J. A., Read, A. M., Milan, S. E., & Palmroth, M. (2016). Modeling the magnetospheric x-ray emission from solar wind charge exchange with verification from XMM-Newton observations. *Journal of Geophysical Research: Space Physics*, *121*(5), 4158–4179. <https://doi.org/10.1002/2015JA022292>
- Yan, G., Liu, Z., Shen, C., Dunlop, M., Balogh, A., Rème, H., et al. (2009). Solar wind entry via flux tube into magnetosphere observed by cluster measurements at dayside magnetopause during Southward IMF. *Science in China - Series E: Technological Sciences*, *52*(7), 2104–2111. <https://doi.org/10.1007/s11431-009-0088-2>
- Zhang, Y., Sun, T., Carter, J. A., Sembay, S., Koutroumpa, D., Ji, L., et al. (2023). Dynamical response of solar wind charge exchange soft X-ray emission in Earth's magnetosphere to the solar wind proton flux. *The Astrophysical Journal*, *948*(1), 69. <https://doi.org/10.3847/1538-4357/ac326>
- Zhang, Y., Sun, T., Wang, C., Ji, L., Carter, J. A., Sembay, S., et al. (2022). Solar wind charge exchange soft X-ray emissions in the magnetosphere during an interplanetary coronal mass ejection compared to its driven sheath. *The Astrophysical Journal Letters*, *932*(1), L1. <https://doi.org/10.3847/2041-8213/ac7521>